

Generation of internal tidal beam in Tasman Sea

September 26, 2018

Abstract

Macquarie Ridge south of New Zealand is a moderate generator of internal tidal waves (ITs) forming a tidal beam. The beam was subject to study of TTIDE/TBEAM field program. Here, beam's generation and characteristics are investigated by means of numerical experiments with prescribed different mesoscale conditions. At the strongest site, conversion of barotropic tidal produce on average 1.6 GW of baroclinic mode-1 and with a range of 30 %. This variation is mainly associated with amplitude of remote ITs originating on slopes of Campbell Plateau. The two almost parallel conversion sites form a system similar to a semi-enclosed resonator. Its efficiency of energy extraction is shown to depend on local stratification by (a) changing WKB-scaled topography and (b) phase lag between the sites. The produced baroclinic waves are radiated into deep ocean as a spatially tight beam. Obtained here far-field energy characteristics (152° and 4 kW/m) are in a good agreement with previously reported altimeter and in-situ observations. Though, the numerical experiments points to spatial variation. These modulations arise from interference with intricate wave field setting in due to reflection from Tasmania and multiple generators found throughout Tasman Basin. Among experiments variability arises both due to spatial changes of production hot spots along Macquarie Ridge and interaction with mesoscale eddies found near Tasmania. Effect of the former process is estimated by a semi-analytical model. Besides a

direct dependence of baroclinic tide amplitude on conversion magnitude, its spatial distribution can modulate beam heading by $\pm 3^\circ$ which results in far-field position shifts. (No ending, no strong statement so far). Macquarie Ridge, Tasman Basin where the, where not.

1 Introduction

Baroclinic semidiurnal tides originate as a strong barotropic flow along topography forces heaving of isopycnal surfaces. This process renders scattering of barotropic tidal energy into baroclinic motions (Hendershott, 1981). The so dispersed energy constitutes a third of global budget for lunar semidiurnal constituent (Egbert and Ray, 2000; Munk, 1997) and contributes significantly to internal wave climate (ref?). At most conversion sites because of highly inclined slopes, internal waves of tidal period (internal tides) are radiated as low baroclinic mode. Due to their large length scales decay rates are subtle. This makes low mode tide efficient in carrying baroclinic energy (kinetic?) over distances comparable to size of ocean basins. While generation sites were identified (Morozov, 1995; Simmons et al., 2004; Arbic et al., 2010; Zhao et al., 2016), some were studied in detail (Rudnick et al., 2003; Klymak et al., 2011; Althaus et al., 2003) and analytical models have been developed (Garrett and Kunze, 2007), little is known on how fast and where internal tidal energy is dissipated (deposited). A lot of uncertainty arises because of close relation between the waves and the dynamical oceanic medium, so the wave field is subject to continuous change.

Water column stratification directly impacts internal wave dispersion. In fact, analytical models of generation emphasize a ratio between angle of internal wave characteristics to bathymetric slope (Garrett and Kunze, 2007) along with a height of topography as primary quantities in setting conversion levels (Llewellyn Smith and Young, 2003; Pétrélis et al., 2006). For tall, steeply inclined submarine ridges the energy transfer approaches an upper theoretical limit (Pétrélis et al., 2006; St Laurent et al., 2003) making them to be “oases”

of barotropic tide scattering and internal tide production (Morozov, 1995; Egbert and Ray, 2000). Clearly, the energy rates can be modulated by changing buoyancy frequency (Holloway and Merrifield, 1999), especially when seasonal transformation of water properties happens at same depths as the steepest bottom gradients (Gerkema et al., 2004). Nevertheless, in later field studies it was realized that presence of external baroclinic tidal signal leads to even larger temporal variability (Kelly and Nash, 2010; Zilberman et al., 2011; Pickering et al., 2015). This might occur as opposite ridge slopes affect each other (Nash et al., 2004; Zilberman et al., 2011; Echeverri and Peacock, 2010) or due to spatially inhomogeneous distribution of production hotspots (Osborne et al., 2011; Ponte and Cornuelle, 2013)¹, or as separate topographic features mediate each others generation energy levels (Xing and Davies, 1998; Buijsman et al., 2012,0). This study addresses temporal and spatial variability of tide production happening at Macquarie Ridge, south from New Zealand. Quick recourse to a map of Tasman Sea (Fig. 1) suggests that location of major sea bottom features leads to complex internal tide regime representative both of Kaena Ridge and Luzon Strait. Macquarie Ridge emits energy forming a spatially confined beam (Simmons et al., 2004; Zhao et al., 2016). This is an ubiquitous characteristic of low mode internal tide propagation in the deep ocean that is thought to be a result of multiple source interference (Rainville et al., 2010). The Tasman beam carries away most of the conversed energy and partly deposits it on Tasmanian continental slope found $\sim 1000\ km$ from the ridge. To detail contributing (concurrent) physical processes several field experiments (TBEAM/TTIDE/Tshelf) were conducted (Pinkel et al., 2015) along with an investigation of satellite altimetry observations (Zhao et al., 2018). The latter results were favorably compared to averaged in-situ measurements (Waterhouse et al., 2018) corroborating (existence of?) northwesterly propagating low mode beam of small decay rate. Nevertheless, the observed temporal variability of the beam's heading and amplitude needs an interpretation to restrain boundary conditions for a problem of shoaling (scattering and reflection?) internal tide on three dimensional topog-

¹there should a verb here, needs to be restructured

raphy and consequent energy dissipation (Klymak et al., 2016).

The non-stationary behavior in propagation of the baroclinic tidal waves results from interaction with varying oceanographic conditions (e.g., Mooers, 1975). Depending on involved length scales and magnitudes, different regimes can be realized (Bühler, 2014)². On the first order, when the (wave-flow) scales are largely detached as in geometric optics limit, the oceanic conditions simply change mode-1 phase speed and cause wave front refraction (Rainville and Pinkel, 2006; Zaron and Egbert, 2014; Kelly and Lermusiaux, 2016). The phenomena is augmented in presence of considerable mean flows with vertical structure (Park and Watts, 2006; Buijsman et al., 2017). This can further produce non negligible Doppler shifting (Chavanne et al., 2010) and shifts of apparent wave frequency in strong vortical flows (Kunze, 1985). In the higher orders, nonlinear interactions lead to scattering into high modes (Dunphy and Lamb, 2014), directional spreading (Wagner et al., 2017; Dunphy et al., 2017) and nonintuitive energy transfers via resonant triad interactions with geostrophic turbulence (Ward and Dewar, 2010). Still in typical oceanographic setting the first order mechanisms are the most widespread (Kelly and Lermusiaux, 2016; Zaron and Egbert, 2014). The latter work as well investigated role of generation in the producing time variable far-field. This was hypothesized by (Wunsch, 1975) who suggested that “energetic beams will be moved comparatively large distances by small changes in angle and may be missed by isolated instruments” ³.

In the setting of Tasman Sea both phenomena are plausible reasons to produce the documented variation in incidence of the low mode tidal beam on Tasman continental slope. To identify cause-and-effect relationship numerical experiments are carried out with different conditions of the oceanic medium (Section 2). Variable levels of internal tide production are examined in Section 3a and resultant beam’s characteristics are quantified in its traverse of Tasman Basin (Section 3b). These results are brought together to be studied in terms of a semi-analytical generation model and action of mesoscale (Section 4a). This helps to

²I didn’t read Buhler, 2014 book, just he discusses in great detail the topic

³this is a direct quote, marks are ok?

provide context for the field observations (Section 4b). This follows by conclusions. And in the Appendices mathematical nuances are described in greater detail.

2 Numerical experiments and analysis

2.1 Numerical experiments

To study variability of internal tide generation around New Zealand and its propagation numerical simulations were performed with Regional Ocean Modeling System (Shchepetkin and McWilliams, 2005). The numerical domain covered southern Tasman Sea from subantarctic waters of 60° S to subtropics in 35° S. And the zonal extent stretched from 142° to 172° E. This ensued correct representation of reach regional oceanographic conditions. The horizontal grid spacing was taken to be of $1/32^{\circ}$ corresponding on average to discretization of 3 km in zonal direction and 2.5 km in meridional. The nonuniformly separated, vertical 50 *s*-levels were placed to smoothly follow subsurface terrain.

Such discretization of vertical momentum equation tends to induce artificial, horizontal along-slope flows (Haidvogel and Beckmann, 1999) due to errors in reproducing of pressure gradient force. Especially severe errors are made by steep terrain. The misbehavior is usually solved by aritificial smoothing of topography. This procedure additionally increases numerical stability, but has an adverse effect on internal tide generation (Di Lorenzo et al., 2006) since primary production sites are collocated with large topographic gradients. To test the numerical setup, a sensitivity study was carried out with simulations of $1/8^{\circ}$, $1/16^{\circ}$, $1/64^{\circ}$ horizontal resolution. The essential for this study internal tide behavior manifested at $1/16^{\circ}$ and converged for $1/32^{\circ}$ and $1/64^{\circ}$ cases. There no marked differences were observed, except a substantial increase in high mode content which is in line with ⁴ (Di Lorenzo et al., 2006). This work addresses the gravest baroclinic mode dynamics in the deep ocean. Spatial extent of waves is large compared to associated vertical displacements. This ensures linear regime of propagation without dispersive and nonhydrostatic effects taken place such as fission into solitons. A hydrostatic solver used in ROMS seems to be a proper choice for the simulations. Such simplification in wave dynamics was assumed in previous studies ((Carter

⁴previous investigations

et al., 2008; Merrifield et al., 2001; Merrifield and Holloway, 2002; Kerry et al., 2013)). In more dynamically accurate simulations of (Kang and Fringer, 2012; Zhang et al., 2011) the nonhydrostatic effects are found to be important only for internal tides in shallow waters, while for main part generation follows linear dynamics with vertical accelerations to have a negligible contribution.

The horizontal boundary conditions were imposed to be open for depth-averaged, barotropic flows following recommendations proposed by (Marchesiello et al., 2001). The baroclinic fields are nudged to zero by linear increased lateral viscosity and diffusivity over sponge layers. Through the same outer boundaries numerical simulations were forced with barotropic tide. The tidal currents and sea level are derived from TPXO atlas, version 7.2 (Egbert and Erofeeva, 2002) and prescribed as linearly interpolated volume transports. It was used only the largest semidiurnal constituent M_2 . Amplitude ratio between the principal lunar and solar components are 4-to-1 suggestive of slight open-ocean spring-neap modulation. The diurnal species are weak in the region except shoals east of New Zealand (Walters et al., 2001).

To investigate variations of baroclinic tide dynamics several ocean states were prescribed and analyzed separately. In the simplest setting lateral gradients in water properties were absent, while buoyancy frequency was set to representative of Tasman Basin. The second set of simulations was comprised to investigate interannual and interseasonal variability (Table 1). And the third calculation was intended to cover period of TTIDE/TBEAM/Tshelf field programs (Pinkel et al., 2015), a single experiment once initialized was left to proceed for three numerical months. The simulations with variable conditions were at first initialized by HYCOM hindcasts⁵ for respective start date. Then during integration, along with barotropic tidal flow, time-variable, subtidal two dimensional fields⁶ of horizontal currents, temperature and salinity were imposed onto the numerical ocean. The air-sea interaction obtained from MERRA-reanalysis (Rienecker et al., 2011) was also given by insolation, air

⁵(NAVGEN; downloaded from hycom.org)

⁶(vertical coordinate and along boundary coordinate)

Table 1: Carried out numerical experiments

Numerical experiments used in this study		
Experiment abbreviation	Simulation period	Comments (reason?)
Uniform		No mesoscale
2012	Jan 1st - Jan 15th, 2012	Interannual
2013	Jan 1st - Jan 15th, 2013	Interannual
2014	Jan 1st - Jan 15th, 2014	Interannual
2013_Oct	Oct 1st - Oct 15th, 2013	Interseaonal
2015_Mar	Mat 1st - Mar 15th, 2015	Interseaonal
2015_TTIDE*	Jan 1st - Mar 1st, 2015	Field period

* the results are named as respective day of year over which post-analysis was performed, e.g. *d20 – 25*

temperature, EP rates and most importantly, wind stresses.

2.2 Internal tide analysis

As it is seen in table 1, the simulations were carried out for 15 days or longer. The first 10 days were left for spin up of baroclinic tide generation and propagation. Roughly, it takes about 7 days for the mode-1 signal to traverse Tasman Sea from New Zealanda to Tasmania. After that period, three dimensional fields of velocity, temperature and salinity were sampled hourly. These were later subject to high pass filtering with Butterworth filter of order 6 with cut off time of 36 hours. This removed subtidal motions and left out signal was further fit in a least square sense to the principle semidiurnal harmonic. Then the three dimensional fields underwent a separation into barotropic and baroclinic signals (Cummins and Oey, 1997; Kunze et al., 2002; Carter et al., 2008). A depth-averaged current is thought to represent a pure barotropic signal and any vertical deviation is attributed to a baroclinic wave,

$$\vec{u}_{bt}(x, y) = \frac{1}{H} \int_{-H}^0 \vec{u}(x, y, z) dz, \quad \vec{u}_{bc}(x, y, z) = \vec{u}(x, y, z) - \vec{u}_{bt}(x, y) \quad (1)$$

To describe distribution of pressure, at first, from a linear equation of state and respective *TS*-fields density perturbation from the reference is found. Then the hydrostatic approximation is employed and after vertical integration the total pressure field is found. This is

then subject to baroclinicity condition, so that baroclinic pressure anomaly is taken to be a deviation from the depth-averaged,

$$p(x, y, z) = \int_{-z}^0 \rho(x, y, z) dz, \quad p_{bc}(x, y) = p(x, y, z) - \frac{1}{H} \int_{-H(x,y)}^0 \rho(x, y, z) dz \quad (2)$$

In the both expressions rigid-lid approximation is used. This is a valid statement unless vertical accelerations are smaller than acceleration due to gravity which is true except shallow depths (Kelly et al., 2010).

Each dynamical variable was then decomposed into vertical modes. The structure functions were obtained from local Brunt-Vaisala frequency profiles found from time-averaged density fields. These were used in Sturm-Liouville problem for the hydrostatic approximation,

$$\frac{d}{dz} \left(\left(\frac{\omega^2 - f^2}{N^2} \right) \frac{d\psi(z)}{dz} \right) + c_n^2 \psi(z) = 0 \quad (3)$$

where c_n is the mode phase speed in nonrotating ocean. The first 3 vertical modes were fit into three-dimensional fields. And only mode-1 was used in the following results.

Now energy diagnostics could be obtained. First, depth-averaged mode-1 energy flux is

$$\vec{F} = \frac{1}{2} \frac{1}{H} \vec{u}^* p \int_{-H}^0 \psi_1(z) \psi_1(z) dz \quad (4)$$

At second, rates of conversion from barotropic to baroclinic (Simmons et al., 2004; Kurapov et al., 2003) were calculated as

$$C_{bt \rightarrow 1} = -\frac{1}{2} (\vec{u}_{bt}^* \cdot \nabla H) p_{1, \text{bot}} \quad (5)$$

The fraction $\frac{1}{2}$ in front of the energy characteristics appear because harmonic, complex amplitudes are used in the expressions.

These calculations had produced a set of dynamical variables of barotropic and baroclinic

fields in each experiment. The obtained values per experimenter hereafter will be referred as a realization. For instance, the longest experiment, 2015_TTIDE had 10 realizations. To study variability of the system, mean values were defined as arithmetic mean,

$$\langle \bullet \rangle = \frac{1}{N} \sum_i \bullet_i \quad (6)$$

where \bullet a field being averaged and N is a number of experiments used. The variation between realizations is studied by mean deviation,

$$\Delta \bullet = \frac{1}{N} \sum_i (\bullet_i - \langle \bullet \rangle) \quad (7)$$

2.3 Discrete Fourier Decomposition by inverse modeling

⁷ In addition to the above characteristics the mode-1 internal tide field was subject to directional analysis in order to remove interference modulations. Similar methods were used previously in internal tide field programs (Hendry, 1977; Lozovatsky et al., 2003)⁸ or satellite altimetry (Dushaw, 2002) or in surface wave studies (Longuet-Higgins, 1961; Munk et al., 1963; Long, 1986). Let mode-1 pressure in complicated seas to be described by an angular spectrum

$$p(\vec{r}, t) = \int_0^{2\pi} d\theta_k S(\theta_k) e^{i\vec{k}(\theta_k) \cdot \vec{r} + \phi(\theta_k) - i\omega t} \quad (8)$$

Here each elementary (monochromatic) sine wave of wavenumber k travels in direction θ with energy $S(\theta)^2 d\theta$ and temporal (spatial) lag of $\phi(\theta)$. The statement can be reformulated in terms of Fourier coefficients (Munk et al., 1963) by application of Jacobi-Anger expansion,

$$p(r, \theta) = e^{i\vec{k}(\theta) \cdot \vec{r}} = \sum_{m=-\infty}^{m=\infty} i^m J_m(kr) e^{im(\theta - \theta_k)} \quad (9)$$

⁷I will move it to Appendix and will leave just a paragraph or two

⁸that were based on array beamforming method and stationarity of the field

shows that a field at point (r, θ) produced by plane wave can be expanded in series of Bessel functions and circular functions. Then its substitution into (8) and reorganization lead to

$$p(r, \theta) = \sum_{m=-\infty}^{m=\infty} \left[\int_0^{2\pi} d\theta_k S(\theta_k) e^{i\phi(\theta_k)} e^{-im\theta_k} \right] i^m J_m(kr) e^{im\theta} \quad (10)$$

Term in brackets (square brackets) represent convolution integrals defining Fourier coefficients of order m , $A_m - iB_m$. Thence, series (??) state a model equation to find the unknown coefficients from the known, measured pressure field that were sampled at a set of points (r_i, θ_i) and if infinite series is truncated at some order N . Real and imaginary parts will constitute two separate problems allowing deterministic definition of the spectrum. The same steps are repeated but with current velocities instead. Plane wave polarization relations (e.g., Müller and Liu, 2000) are inserted into (8) and the following equations are found,

$$\begin{Bmatrix} u_i \\ v_i \end{Bmatrix} = \frac{1}{2} \sum_{m=-N}^{m=N} J_m(kr_i) e^{im(\theta+\pi/2)} \begin{Bmatrix} (\omega - f)A_{m+1} + (\omega + f)A_{m-1} - i[(\omega - f)B_{m+1} + (\omega + f)B_{m-1}] \\ (\omega - f)B_{m+1} - (\omega + f)B_{m-1} + i[(\omega - f)A_{m+1} - (\omega + f)A_{m-1}] \end{Bmatrix} \quad (11)$$

The dependence of currents on wave bearing causes splitting of Fourier coefficients and asymmetry via Coriolis effect. This results points out that to describe velocity field higher circular harmonics have to be used. Physically, velocity field has higher spatial wavenumber. But in (11) additionally, the asymmetry is observed for clockwise and counterclockwise components.

The inverse model combines dynamical relations of (10) and (11) into a matrix equation

$$y = Kx \quad (12)$$

Generally, it is unstable to small errors in data and produce physically inconsistent results. This can be circumvented by seeking a damped least square solution (Munk et al., 2009) where a minimization function is given by

$$J = \|Kx - y\|_2^2 + \alpha\|x\|_2^2 \quad (13)$$

The unknown regularization parameters α acts as a high-pass filter in a singular value decomposition of K (Bennett, 1992). In field studies this is usually set by a signal-to-noise ratio (Munk et al., 2009), since the parameter scales noise variance (residue) to actual signal's strength. To obtain α in data-driven way a straightforward approach is adapted that based on trade-off curve method (Hansen and OLeary, 1993). In (13) amount of allowed error is competing with solution's variance. An optimal parameter should balance these factors. This is seen as a rapid change in behavior of curve associating residue with model's norm as regularization varies. In most cases the curve has a sharp corner connecting aforementioned limits, hence, the method's name is a L-curve (Hansen, 1999). And the corner is to occur for an optimal regularization parameter.

The equations (10) and (11) are sampled at locations in a concentric arrays placed at λ , 0.5λ , 0.25λ where λ is a local mode-1 wavelength. At each location u , v , p are used as data and for a region embraced by array Fourier coefficients are found. And these then are used in reconstructions.

The method used here is different from (Zhao et al., 2010) for two main reasons. The model equations produce simultaneous fit of all the components, rather than a finite number of a single directed plane waves. This can make a difference in regions where diffraction is important such as near internal tide generation or scattering regions. And at second, velocity field is utilized which provides an additional constraint. Moreover, in synthetic experiments with (13) where instead of $L2$ -norm regularization it was used $L1$ -norm, the results were approaching one of plane wave technique of (Zhao et al., 2010). Additionally, the proposed

method can be utilized for a single mooring where half-space separation is necessary.

3 Results

3.1 Generation of internal tidal beam

Surface tide arrives to Southern Tasman Sea from North (Fig. 2). Its advancement happens in counterclockwise manner with maximum amplitude of sea level located along New Zealand’s coast. This is a typical Kelvin wave behavior (Walters et al., 2001). Also the barotropic tide produces strong currents in shallow Bass Strait, but relatively weak anywhere else in the basin. The simulated sea surface tidal oscillation closely follows TPXO atlas with gross features well captured. Presence of baroclinic field manifests in perturbation of sea level magnitude and cotidal lines. In the basin this have a striking wavy character. This corresponds to propagation of low mode tidal wave (Fig. 3).

The baroclinic tidal field represents a complex pattern produced by multiple generation sites defined by steep topography. Primary production sites are just south of New Zealand. Here barotropic Kelvin wave faces prominent Macquarie Ridge stretched for 2000 km. As barotropic current decays away from the coastline conversion lessens as well. Nevertheless, low-mode beams are emitted from many locations. Major conversion happens at 49.5° shedding away the strongest beam. This and two nearby beams were identified in altimetric observations (Zhao et al., 2018). Henceforth, analysis is concentrated on the most energetic, central beam.

The central beam is produced by tidal currents impinging on supercritical bathymetry (Fig. 4). Depth of the highest conversion is between 1000-3000 m and spatially confined to two seamounts that are separated with a sill. It has less inclined slopes and plays lesser role in production of the tidal beam. On average, this region of Macquarie Ridge converts 1.6 GW of surface tide. This is half of production of Kaena Ridge, Hawaii (Carter et al., 2008) and much less than Luzon Strait (). Pattern of conversion (Fig. 4) also exhibits regions of

internal tide destruction produced by complex dynamics caused by superposition. In fact, an oppositely located Aucklands Escarpment presents an important source of baroclinic energy. Fig. 3 clearly illustrates existence of a standing wave in Solanders Trough. The total field is characterized by a node in horizontal kinetic energy with fluxes revolving in counterclockwise direction Fig. 5 because of Southern Hemisphere. By the method proposed in ref-to methods, the standing wave is separated into elemental east-west directed components (Fig. 5). On leeward side of Macquarie Ridge generation occurs at the same seamounts but there is a region of destruction that coincides with incidence of waves emitted by the escarpment. There generation has reacher structure both due to more complicated topography that is crisscrossed by canyons but also because of Macquarie ridge produced waves. Quantifying energy transfer across the trough and comparing with spatially integrated conversion rates points out to fact that wave energy is being recirculated by slope's supercritical reflection and only partly fed by barotropic field. In overall, such system is similar to Luzon strait where resonance conditions exist between two parallel ridges (Buijsman et al., 2014). In case of Macquarie Ridge and Campbell Plateau resonance is only partial since the former has a slant orientation of 15° . Though at 49.5° the distance corresponds to $3/4$ of mode-1 wavelength. Such spacing is sensible to phase lags and can either lead to intensification or destruction of generation. This is illustrated by comparison of two simulations that presents dynamically different regimes of generation.

Conversion rate shows how much work was done by baroptropic tide to displace isopycnal interfaces. This is understood as work against buoyant forces. But it can happen that barotropic forcing will be oppositely directed if somewhere in the water column other forces are present. For case of '2014' simulation (Fig. 6, a-b) during ebb tide on tideward side there is net energy conversion to baroclinic field even that along bottom an internal wave ray is developing by upward displaced interfaces as a result of previous tidal phase. Hence, at these location a newly generated internal wave does work against downward barotropic flow. And this produces negative conversion (Fig. 6, e) at some moment. As tide turns conversion

changes sign again. Overall, period averaged transfer is positive, i.e. surface tide losses energy. In the other experiment presented (d10-15, Fig. 6, c-d), there is an intensification due to advancement of a mode-1 wave. In actuality, its propagation from Solanders Trough (165°) and over the sill is the major difference between two simulations. So in '2015'-setting similar along slope advancement of an internal wave ray is observed, but now due to shoaling mode-1 conversion is positive throughout tidal cycle.

The contrary situation is found on leeward side (164.5°) where surface tide current has the opposite direction. For '2015' it appears that propagating mode-1 is losing energy since it does work against barotropical forcing by dipping isopycnals. Though in transition some energy is lost from surface tide. In '2014' there is a reflection of an internal wave ray as phase is advancing onto the sill. This coincides with upward barotropic flow that in total leads to intensification. In total, period averaged conversions have different signs on leeward side. Comparison of mode-1 wave position in the trough at ebb tide (Fig. 6, a,c) suggests difference in timing of the remote wave arrival or its advancement. This is explored on (Fig. 6, g). The total signal shows a region of low phase change eastward of 165° that corresponds to concentration of kinetic energy (Fig. ??, a). Decomposition of the signal presents it roughly as a sum of the ridge generated waves (eastward propagation) and the escarpment originated (westward) waves. The actual relation will depend on relative magnitudes (Martini et al., 2007). But westward of 165° there is almost a free propagation in '2015' of the "escarpment" waves as the total signal closely corresponds to them. But in '2014' due to sills generation and strong reflection, phase difference with local barotropic tide falls below 90° , so that there is an intensification of generation.

The described situation provides a several approaches to narrate variability in conversion rates. At first, it is clear that amount of remote energy crossing Macquarie Ridge through the sill will shape the overall conversion. Hence, energy incident from leeward side can provide such estimate. It is quantified from the numerical simulations by line-integration of energy fluxes through leeward side (Fig. 4). Additionally, this amount is modulated by

reflection of the sill. Here it is thought as a knife-edge barrier for which reflectivity was analytically found by (Larsen, 1969) with similar investigations of (Klymak et al., 2013). Sill's depth is obtained as a depth jump from the trough to the sill that were WKB-scaled. The resultant calculation is given by (Fig. 7, a) where total conversion of tideward side of Macquarie Ridge is plotted against amount of transmitted mode-1 energy. At second, efficiency of generation will depend on phase difference between the remote waves and local forcing. This is estimated from mode-1 eigenspeed for Solanders Trough. Taken distance separating Macquarie Ridge and Aucklands Escarpment to be about 115 *km* (average mode-1 wavelength 155 *km*), the time to cross the trough can be found (Fig. 7, b). And additional factor is environmental changes that are associated with overall efficiency of generation by the ridge. Again by applying WKB-scaling variation of ridge's depth relative to the surrounding deep ocean is found and then scaled to converted energy by application of theory by (St Laurent et al., 2003). The mean barotropic current of 0.03 *m/s* generation was considered to produce (Fig. 7, c).

The linear regression for the first parameters has correlation coefficient R^2 slightly higher than 0.5, and for linear multiple variable regression it increases to 0.7. The least dependence is found for stratification variability on the tideward side. Though if all three parameters combined R^2 becomes 80%. Hence, most variability is associated with leeward dynamics and not local stratification. Additionally, all three environmental parameters do not always change in similar fashion suggestive for different mesoscale dynamics occurring in the deep sea, over Macquarie Ridge and in Solanders Trough. This is not surprising since the region is affected by frontal zone and reach in subtidal dynamics (Smith et al., 2013). Further, inclusion of transmission coefficient increases correlation, but most variability comes from amount of energy traveling from Aucklands Escarpment (Fig. 5, c). This is much harder problem to estimate since generation in that region has much more spotty character (Fig. 4) because of complex topography and large influence of eastward traveling waves which can also act either to intensify local generation or destroy baroclinic tides.

3.2 Characteristics of Tasman tidal beam

Widespread energy conversion at Macquarie Ridge produce a clearly defined internal tidal beam (Fig. 3). To delineate spatial variability of energy characteristics, their cross-beam averages are introduced (Fig. 3); and to investigate respective temporal variations, ensemble-means and standard deviations are reported. It is worth noting that while ensemble-mean allows a straightforward interpretation of mode-1 dynamics, it will incorporate a portion of variable (non-stationary) signal since any energy characteristic is a nonlinear quantity (Zaron and Egbert, 2014). On contrary, for instance, a flux found from ensemble-mean pressure and currents will exclusively provide a stationary part. Yet if a mode-decomposed signal is considered, finding the means will entail averaging of vertical basis functions. As a consequence, their orthogonality will not be preserved leading to ambiguity in dynamics. Henceforth, an ordinary mean over realizations of beam’s energetics is considered. Performed comparison (not shown) between an ensemble-mean of flux and a flux of ensemble-mean did not reveal significant differences in spatial structure, though magnitude of latter was roughly half smaller.

The spatial-temporal changes are provided by Fig. 8. Dashed lines mark second-order polynomial fits (Zhao et al., 2018) used to remove along-beam oscillations. On average, the central beam leaves Macquarie Ridge carrying away 1.6 GW in mainly western direction (Fig. 8, (a, b)). In the open ocean, over $\sim 100 \text{ km}$ there is a rapid directional turn, but as the beam progresses, rate of change decreases. The latter regime is an example of refraction (Cummins et al., 2001; Rainville and Pinkel, 2006; Zhao et al., 2018) due to a meridional change of Coriolis parameter and consequently, a phase speed. Same phenomena is also seen in ratio of HKE to APE (Fig. 8, (c)). By Tasmania the beam is oriented in northwestern direction (150° from East) and has more available potential energy (APE) at the expense of horizontal kinetic form (HKE). Additional feature is an energy decay (Fig. 8, (b)) that is caused by geometrical effects and by dynamical processes such as friction and high mode scattering. Amount of deposited energy was determined by flux divergence and on average

comprised 35 % so that the beam brings 1 GW of baroclinic energy to Tasmania.

According to the numerical experiments there is a high degree of spatial variability (Fig. 8). Flux vectors sinuously deviate from the fit by $\pm 30^\circ$. The alterations align with growth or decline in the flux magnitude. While the energy partitioning reversely follows this arrangement. These aspects of propagation are indicative of interference (Martini et al., 2007; Zhao et al., 2010) between the internal tidal beam and remote waves. Fig. 9 attest presence of multi-directional wave field. Its components were extracted by the same method of directional spectra (Appendix A) that was then integrated over 4 circular quadrants. Then for each an ensemble-mean was obtained. The northwesterly traveling waves highlight a plane-wave propagation of the internal tidal beam. This component will be referred as a planar beam. Its total energy is partitioned closely following a theoretical prediction. However, contrary to expected equatorward increase of potential energy, there is a decay that pertains to frictional losses.⁹ Southwesterly waves (Fig. 9, (b)) originate from Lord Howe Rise and Gilbert Seamount. Both are oriented against the surface tide current (Fig. 1) and hence, efficiently scatter the barotropic energy (e.g., Fig. 3). Macquarie Ridge also emits waves traveling in this quadrant. As these signals interfere with the planar beam, the aforementioned rapid directional turn close to the ridge can now be easily understood. Further, APE becomes only slightly perturbed, but the ratio clearly demonstrates $\sim 200\ km$ modulations. Overall pattern is further complicated with an addition of southeasterly signals. This introduces another spatial frequency of $\sim 150\ km$ that is affirmed by spatial variation in the potential energy. This irregularity is limited to region $\sim 500\ km$ from Cascade Seamount. Because this topographic feature reflects portion of the internal tidal beam and cause existence of SW waves. Note their tenfold weakness to the planar beam. On the last panel additional source of baroclinic tides is discovered at South Tasman Rise. Obviously, presence of the multiple generation sites leads to existence of “internal tidal swell” (Hendry, 1977) which is not strong, but yet obscures the beam propagation.

⁹Minor oscillations are artifacts of analysis owing to finite size of fitting windows.

The interference will inevitably produce signature in the temporal variability (Fig. 8, purple lines and thin gray lines). Large changes in energy partitioning is collocated with locations of nodes-antinodes. The flux heading has similar pattern, but degree of variability rises as the tidal beam crosses Tasman Basin. Oppositely, the integrated flux alters less between the simulations and any differences are uniformly distributed through the course of propagation. These observations are detailed by Fig. 10 where previous reconstructions are given with addition of temporal variability informed by along-beam distribution of standard deviations and energy flux variance ellipses. The planar beam has mainly magnitude variation that is associated with different conversion levels at Macquarie Ridge. With distance deviations become apparent in energy flux orientation, so that variability ellipses are becoming slanted to the mean vectors. A striking feature is in uniformity of the ellipse distribution and mean vector orientation. This behavior alludes to changes in generation as a cause. Further, inclusion of the swell produces nodes-antinodes so that now energy density variability concentrates near these locations. Contrary, regardless of spatial modulation in the mean flux vector heading, its variability preserves uniformity. But this characteristic is smeared by the reflected, southeasterly waves. Superposition leads to strong modulations in the deviations. Notably, the magnitude variability is not affected on average. Overall, the total field demonstrates high degree of spatial-temporal alterations. Nevertheless, temporal changes accord with the planar beam behavior and all further complexity arises due to multiple-wave interference.

4 Discussion

The spatial-temporal characteristics present a complication for direct interpretation of diagnosed energy quantities in describing the tidal beam. Its properties are obscured due to interference and hence, needs additional inferences. This is related to variability. It is unclear what can produce beam's energy levels and its orientation/position. Two reasons could be named as accumulating interaction with mesoscale field and generation producing.

Table 2: Internal tidal energy flux properties in the far field

Source	Flux [kW/m]	magnitude	Heading [°]
This study - all experiments			No mesoscale
This study - only field period			No mesoscale
Altimetry observations (Zhao et al., 2018)	3.9 ± 2.2		141 ± 2
Field observations (Waterhouse et al., 2018)	3.4 ± 1.4		149 ± 3

Now comparison of the decomposed planar beam can be made with factual observations made by (Waterhouse et al., 2018; Zhao et al., 2018).

5 Conclusions

6 Figures

References

Ttide proposal.

Althaus, A. M., Kunze, E., and Sanford, T. B. (2003). Internal tide radiation from mendocino escarpment. *Journal of Physical Oceanography*, 33(7):1510–1527.

Arbic, B. K., Wallcraft, A. J., and Metzger, E. J. (2010). Concurrent simulation of the eddying general circulation and tides in a global ocean model. *Ocean Modelling*, 32(3-4):175–187.

Bennett, A. F. (1992). *Inverse methods in physical oceanography*. Cambridge university press.

Bühler, O. (2014). *Waves and mean flows*. Cambridge University Press.

Buijsman, M., Uchiyama, Y., McWilliams, J., and Hill-Lindsay, C. (2012). Modeling semidiurnal internal tide variability in the southern california bight. *Journal of Physical Oceanography*, 42(1):62–77.

Buijsman, M. C., Arbic, B. K., Richman, J. G., Shriver, J. F., Wallcraft, A. J., and Zamudio, L. (2017). Semidiurnal internal tide incoherence in the equatorial pacific. *Journal of Geophysical Research: Oceans*, 122(7):5286–5305.

Buijsman, M. C., Klymak, J. M., Legg, S., Alford, M. H., Farmer, D., MacKinnon, J. A., Nash, J. D., Park, J.-H., Pickering, A., and Simmons, H. (2014). Three-dimensional double-ridge internal tide resonance in luzon strait. *Journal of Physical Oceanography*, 44(3):850–869.

Carter, G., Merrifield, M., Becker, J., Katsumata, K., Gregg, M., Luther, D., Levine, M.,

- Boyd, T. J., and Firing, Y. (2008). Energetics of m 2 barotropic-to-baroclinic tidal conversion at the hawaiian islands. *Journal of Physical Oceanography*, 38(10):2205–2223.
- Chavanne, C., Flament, P., Luther, D., and Gurgel, K. (2010). The surface expression of semidiurnal internal tides near a strong source at hawaii. part ii: Interactions with mesoscale currents*. *Journal of Physical Oceanography*, 40(6):1180–1200.
- Cummins, P. F., Cherniawsky, J. Y., and Foreman, M. G. (2001). North pacific internal tides from the aleutian ridge: Altimeter observations and modeling. *Journal of Marine Research*, 59(2):167–191.
- Cummins, P. F. and Oey, L.-Y. (1997). Simulation of barotropic and baroclinic tides off northern british columbia. *Journal of Physical Oceanography*, 27(5):762–781.
- Di Lorenzo, E., Young, W. R., and Smith, S. L. (2006). Numerical and analytical estimates of m 2 tidal conversion at steep oceanic ridges. *Journal of physical oceanography*, 36(6):1072–1084.
- Dunphy, M. and Lamb, K. G. (2014). Focusing and vertical mode scattering of the first mode internal tide by mesoscale eddy interaction. *Journal of Geophysical Research: Oceans*, 119(1):523–536.
- Dunphy, M., Ponte, A. L., Klein, P., and Le Gentil, S. (2017). Low-mode internal tide propagation in a turbulent eddy field. *Journal Of Physical Oceanography*, 47(3):649–665.
- Dushaw, B. D. (2002). Mapping low-mode internal tides near hawaii using topex/poseidon altimeter data. *Geophysical Research Letters*, 29(8).
- Echeverri, P. and Peacock, T. (2010). Internal tide generation by arbitrary two-dimensional topography. *Journal of Fluid Mechanics*, 659:247–266.
- Egbert, G. and Ray, R. (2000). Significant dissipation of tidal energy in the deep ocean inferred from satellite altimeter data. *Nature*, 405(6788):775–778.

- Egbert, G. D. and Erofeeva, S. Y. (2002). Efficient inverse modeling of barotropic ocean tides. *Journal of Atmospheric and Oceanic Technology*, 19(2):183–204.
- Garrett, C. and Kunze, E. (2007). Internal tide generation in the deep ocean. *Annu. Rev. Fluid Mech.*, 39:57–87.
- Gerkema, T., Lam, F.-P. A., and Maas, L. R. (2004). Internal tides in the bay of bisay: conversion rates and seasonal effects. *Deep Sea Research Part II: Topical Studies in Oceanography*, 51(25-26):2995–3008.
- Haidvogel, D. B. and Beckmann, A. (1999). *Numerical ocean circulation modeling*. World Scientific.
- Hansen, P. C. (1999). The l-curve and its use in the numerical treatment of inverse problems.
- Hansen, P. C. and OLeary, D. P. (1993). The use of the l-curve in the regularization of discrete ill-posed problems. *SIAM Journal on Scientific Computing*, 14(6):1487–1503.
- Hendershott, M. C. (1981). Long waves and ocean tides. *Evolution of physical oceanography*.
- Hendry, R. (1977). Observations of the semidiurnal internal tide in the western north atlantic ocean. *Philosophical Transactions of the Royal Society of London A: Mathematical, Physical and Engineering Sciences*, 286(1330):1–24.
- Holloway, P. E. and Merrifield, M. A. (1999). Internal tide generation by seamounts, ridges, and islands. *Journal of Geophysical Research: Oceans*, 104(C11):25937–25951.
- Kang, D. and Fringer, O. (2012). Energetics of barotropic and baroclinic tides in the monterey bay area. *Journal of Physical Oceanography*, 42(2):272–290.
- Kelly, S. and Nash, J. (2010). Internal-tide generation and destruction by shoaling internal tides. *Geophysical Research Letters*, 37(23).

- Kelly, S., Nash, J., and Kunze, E. (2010). Internal-tide energy over topography. *Journal of Geophysical Research: Oceans (1978–2012)*, 115(C6).
- Kelly, S. M. and Lermusiaux, P. F. (2016). Internal-tide interactions with the gulf stream and middle atlantic bight shelfbreak front. *Journal of Geophysical Research: Oceans*, 121(8):6271–6294.
- Kerry, C. G., Powell, B. S., and Carter, G. S. (2013). Effects of remote generation sites on model estimates of m 2 internal tides in the philippine sea*. *Journal of Physical Oceanography*, 43(1):187–204.
- Klymak, J. M., Alford, M. H., Pinkel, R., Lien, R.-C., Yang, Y. J., and Tang, T.-Y. (2011). The breaking and scattering of the internal tide on a continental slope. *Journal of Physical Oceanography*, 41(5):926–945.
- Klymak, J. M., Buijsman, M., Legg, S., and Pinkel, R. (2013). Parameterizing surface and internal tide scattering and breaking on supercritical topography: The one-and two-ridge cases. *Journal of Physical Oceanography*, 43(7):1380–1397.
- Klymak, J. M., Simmons, H. L., Braznikov, D., Kelly, S., MacKinnon, J. A., Alford, M. H., Pinkel, R., and Nash, J. D. (2016). Reflection of linear internal tides from realistic topography: The tasman continental slope. *Journal of Physical Oceanography*, 46(11):3321–3337.
- Kunze, E. (1985). Near-inertial wave propagation in geostrophic shear. *Journal of Physical Oceanography*, 15(5):544–565.
- Kunze, E., Rosenfeld, L. K., Carter, G. S., and Gregg, M. C. (2002). Internal waves in monterey submarine canyon. *Journal of Physical Oceanography*, 32(6):1890–1913.
- Kurapov, A. L., Egbert, G. D., Allen, J., Miller, R. N., Erofeeva, S. Y., and Kosro, P. (2003). The m 2 internal tide off oregon: Inferences from data assimilation. *Journal of Physical Oceanography*, 33(8):1733–1757.

- Larsen, L. H. (1969). Internal waves incident upon a knife edge barrier. In *Deep Sea Research and Oceanographic Abstracts*, volume 16, pages 411–419. Elsevier.
- Llewellyn Smith, S. G. and Young, W. (2003). Tidal conversion at a very steep ridge. *Journal of Fluid Mechanics*, 495:175–191.
- Long, R. B. (1986). Inverse modeling in ocean wave studies. In *Wave dynamics and radio probing of the ocean surface*, pages 571–593. Springer.
- Longuet-Higgins, M. S. (1961). Observations of the directional spectrum of sea waves using the motions of a floating buoy. *Ocean wave spectra*, pages 111–136.
- Lozovatsky, I. D., Morozov, E. G., and Fernando, H. (2003). Spatial decay of energy density of tidal internal waves. *Journal of Geophysical Research: Oceans*, 108(C6).
- Marchesiello, P., McWilliams, J. C., and Shchepetkin, A. (2001). Open boundary conditions for long-term integration of regional oceanic models. *Ocean modelling*, 3(1-2):1–20.
- Martini, K., Alford, M., Nash, J., Kunze, E., and Merrifield, M. (2007). Diagnosing a partly standing internal wave in mamala bay, oahu. *Geophysical Research Letters*, 34(17).
- Merrifield, M. A. and Holloway, P. E. (2002). Model estimates of m2 internal tide energetics at the hawaiian ridge. *Journal of Geophysical Research: Oceans*, 107(C8).
- Merrifield, M. A., Holloway, P. E., and Johnston, T. (2001). The generation of internal tides at the hawaiian ridge. *Geophysical Research Letters*, 28(4):559–562.
- Mooers, C. N. (1975). Several effects of a baroclinic current on the cross-stream propagation of inertial-internal waves. *Geophysical and Astrophysical Fluid Dynamics*, 6(3):245–275.
- Morozov, E. G. (1995). Semidiurnal internal wave global field. *Deep Sea Research Part I: Oceanographic Research Papers*, 42(1):135–148.

- Müller, P. and Liu, X. (2000). Scattering of internal waves at finite topography in two dimensions. part i: Theory and case studies. *Journal of physical oceanography*, 30(3):532–549.
- Munk, W. (1997). Once again: once againtidal friction. *Progress in Oceanography*, 40(1):7–35.
- Munk, W., Worcester, P., and Wunsch, C. (2009). *Ocean acoustic tomography*. Cambridge University Press.
- Munk, W. H., Miller, G., Snodgrass, F., and Barber, N. (1963). Directional recording of swell from distant storms. *Philosophical Transactions of the Royal Society of London A: Mathematical, Physical and Engineering Sciences*, 255(1062):505–584.
- Nash, J. D., Kunze, E., Toole, J. M., and Schmitt, R. W. (2004). Internal tide reflection and turbulent mixing on the continental slope. *Journal of Physical Oceanography*, 34(5):1117–1134.
- Osborne, J., Kurapov, A., Egbert, G., and Kosro, P. (2011). Spatial and temporal variability of the m 2 internal tide generation and propagation on the oregon shelf. *Journal of Physical Oceanography*, 41(11):2037–2062.
- Park, J.-H. and Watts, D. R. (2006). Internal tides in the southwestern japan/east sea. *Journal of Physical Oceanography*, 36(1):22–34.
- Pétrélis, F., Smith, S. L., and Young, W. (2006). Tidal conversion at a submarine ridge. *Journal of Physical Oceanography*, 36(6).
- Pickering, A., Alford, M., Nash, J., Rainville, L., Buijsman, M., Ko, D. S., and Lim, B. (2015). Structure and variability of internal tides in luzon strait*. *Journal of Physical Oceanography*, 45(6):1574–1594.

- Pinkel, R., Alford, M., Lucas, A., Johnson, S., MacKinnon, J., Waterhouse, A., Jones, N., Kelly, S., Klymac, J., Nash, J., et al. (2015). Breaking internal tides keep the ocean in balance. *Eos, Trans. Amer. Geophys. Union*, 96.
- Ponte, A. L. and Cornuelle, B. D. (2013). Coastal numerical modelling of tides: Sensitivity to domain size and remotely generated internal tide. *Ocean Modelling*, 62:17–26.
- Rainville, L., Johnston, T. S., Carter, G. S., Merrifield, M. A., Pinkel, R., Worcester, P. F., and Dushaw, B. D. (2010). Interference pattern and propagation of the m 2 internal tide south of the hawaiian ridge. *Journal of Physical Oceanography*, 40(2):311–325.
- Rainville, L. and Pinkel, R. (2006). Propagation of low-mode internal waves through the ocean. *Journal of physical oceanography*, 36(6):1220–1236.
- Rienecker, M. M., Suarez, M. J., Gelaro, R., Todling, R., Bacmeister, J., Liu, E., Bosilovich, M. G., Schubert, S. D., Takacs, L., Kim, G.-K., et al. (2011). Merra: Nasas modern-era retrospective analysis for research and applications. *Journal of climate*, 24(14):3624–3648.
- Rudnick, D. L., Boyd, T. J., Brainard, R. E., Carter, G. S., Egbert, G. D., Gregg, M. C., Holloway, P. E., Klymak, J. M., Kunze, E., Lee, C. M., et al. (2003). From tides to mixing along the hawaiian ridge. *science*, 301(5631):355–357.
- Shchepetkin, A. F. and McWilliams, J. C. (2005). The regional oceanic modeling system (roms): a split-explicit, free-surface, topography-following-coordinate oceanic model. *Ocean modelling*, 9(4):347–404.
- Simmons, H. L., Hallberg, R. W., and Arbic, B. K. (2004). Internal wave generation in a global baroclinic tide model. *Deep Sea Research Part II: Topical Studies in Oceanography*, 51(25):3043–3068.
- Smith, R. O., Vennell, R., Bostock, H. C., and Williams, M. J. (2013). Interaction of the

- subtropical front with topography around southern new zealand. *Deep Sea Research Part I: Oceanographic Research Papers*, 76:13–26.
- St Laurent, L., Stringer, S., Garrett, C., and Perrault-Joncas, D. (2003). The generation of internal tides at abrupt topography. *Deep Sea Research Part I: Oceanographic Research Papers*, 50(8):987–1003.
- Wagner, G. L., Ferrando, G., and Young, W. R. (2017). An asymptotic model for the propagation of oceanic internal tides through quasi-geostrophic flow. *Journal of Fluid Mechanics*, 828:779–811.
- Walters, R. A., Goring, D. G., and Bell, R. G. (2001). Ocean tides around new zealand. *New Zealand Journal of Marine and Freshwater Research*, 35(3):567–579.
- Ward, M. L. and Dewar, W. K. (2010). Scattering of gravity waves by potential vorticity in a shallow-water fluid. *Journal of Fluid Mechanics*, 663:478–506.
- Waterhouse, A. F., Kelly, S. M., Zhao, Z., MacKinnon, J. A., Nash, J. D., Simmons, H., Brahznikov, D., Rainville, L., Alford, M., and Pinkel, R. (2018). Observations of the tasman sea internal tide beam. *Journal of Physical Oceanography*, (2018).
- Wunsch, C. (1975). Internal tides in the ocean. *Reviews of Geophysics*, 13(1):167–182.
- Xing, J. and Davies, A. M. (1998). A three-dimensional model of internal tides on the malin-hebrides shelf and shelf edge. *Journal of Geophysical Research: Oceans*, 103(C12):27821–27847.
- Zaron, E. D. and Egbert, G. D. (2014). Time-variable refraction of the internal tide at the hawaiian ridge. *Journal of Physical Oceanography*, 44(2):538–557.
- Zhang, Z., Fringer, O., and Ramp, S. (2011). Three-dimensional, nonhydrostatic numerical simulation of nonlinear internal wave generation and propagation in the south china sea. *Journal of Geophysical Research: Oceans*, 116(C5).

- Zhao, Z., Alford, M. H., Girton, J. B., Rainville, L., and Simmons, H. L. (2016). Global observations of open-ocean mode-1 m2 internal tides. *Journal of Physical Oceanography*, 46(6):1657–1684.
- Zhao, Z., Alford, M. H., MacKinnon, J. A., and Pinkel, R. (2010). Long-range propagation of the semidiurnal internal tide from the hawaiian ridge. *Journal of Physical Oceanography*, 40(4):713–736.
- Zhao, Z., Alford, M. H., Simmons, H. L., Brazhnikov, D., and Pinkel, R. (2018). Satellite investigation of the m2 internal tide in the tasman sea. *Journal of Physical Oceanography*, 48(3):687–703.
- Zilberman, N., Merrifield, M., Carter, G., Luther, D., Levine, M., and Boyd, T. J. (2011). Incoherent nature of m 2 internal tides at the hawaiian ridge. *Journal of Physical Oceanography*, 41(11):2021–2036.

List of Figures

1	Domain of numerical simulations with geographical locations used in the text	21
2	Comparison of M_2 sea level oscillations simulated by ROMS (left panel) with TPXO-model (right panel).	22
3	Beam of Tasman Sea with major internal tide production sites identified by superposed heat map.	23
4	Generation of internal tides at Macquarie Ridge. (a) The heatmap illustrates criticality in the region of major generation. And ellipses are representative of barotropic current. (b) The diagnosed conversion rates for 'uniform' experiment. The boxes outline regions used in further analysis. (c) Variability of conversion rates in the three regions identified on the previous panel.	24
5	Standing wave between Macquarie Ridge and Auckland Escarpments. (a) Distribution of horizontal kinetic energy in 'uniform' simulation with overlaid energy flux of total mode-1 field. (b) Energy flux map of the westward component and the eastward component (c). Variation in energy characteristics of mode-1 field between Macquarie Ridge and Aucklands Escarpment. The integrated flux was obtained for a dashed transect in (c) and is given by arrows. Dots show conversion rates spatially integrated over boxes given on (Fig. 4, b).	25
6	Distribution of baroclinic fields during ebb and slack tide along transect crossing Macquarie Ridge on Fig. 4, (b). (a-d) Baroclinic pressure anomaly with superposed isopycnal displacements given by contour lines. Positive color is assigned to lifted interfaces and negative - for the opposite. Stick lines show currents. And white line is distribution of barotropic velocity. The tide-ward and leeward sides of Macquarie Ridge are identified by vertical solid and dashed lines. On (e) it is shown time progression of barotropic-to-baroclinic conversion for both experiments and ridge sides. While (f) gives distribution of period averaged conversion rate along the transect. The same is for (g) where progression of mode-1 baroclinic pressure is shown by phases of total field and elemental components. The phases are referenced to flood current across the sill.	26
7	Variation of the tideward conversion rates in relation to mode-1 energy transmitted across the sill (a), to travel time across Solanders Trough (b), to knife-edge barrier representative of Macquarie Ridge seeing from the deep ocean.	27
8	Along beam variation of across averaged energy characteristics. For all panels - solid black line is mean value and thin gray lines for each particular realization. Purple lines show mean deviation of realizations for mean. (a) Direction of energy flux. The dashed line is produced by regression with second order polynomial. (b) Integrated flux carried by the beam. Here the dashed line shows mean integrated flux with no account for relative angle with respect to across beam surface. (c) Ratio between horizontal kinetic energy to available potential energy. The dashed line is the ratio for a plane wave.	28
9	Superposition of multiple waves.	29
10	Variation of the beam.	30
11	Variation of beam parameters.	31

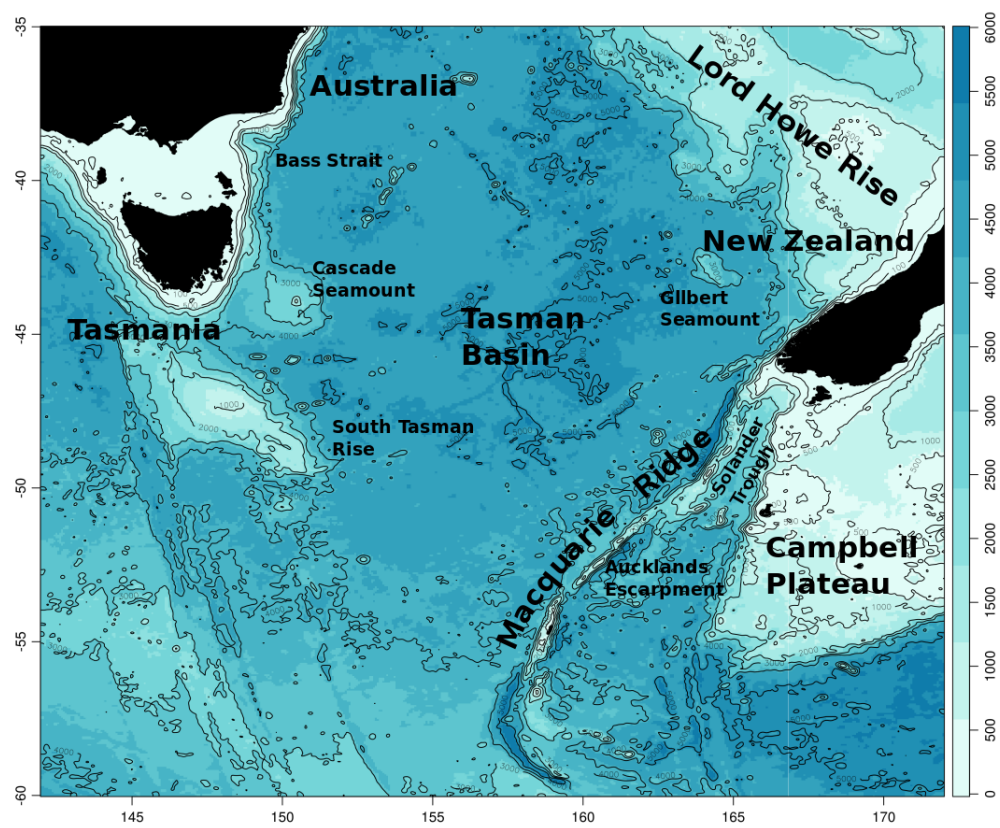


Figure 1: Domain of numerical simulations with geographical locations used in the text

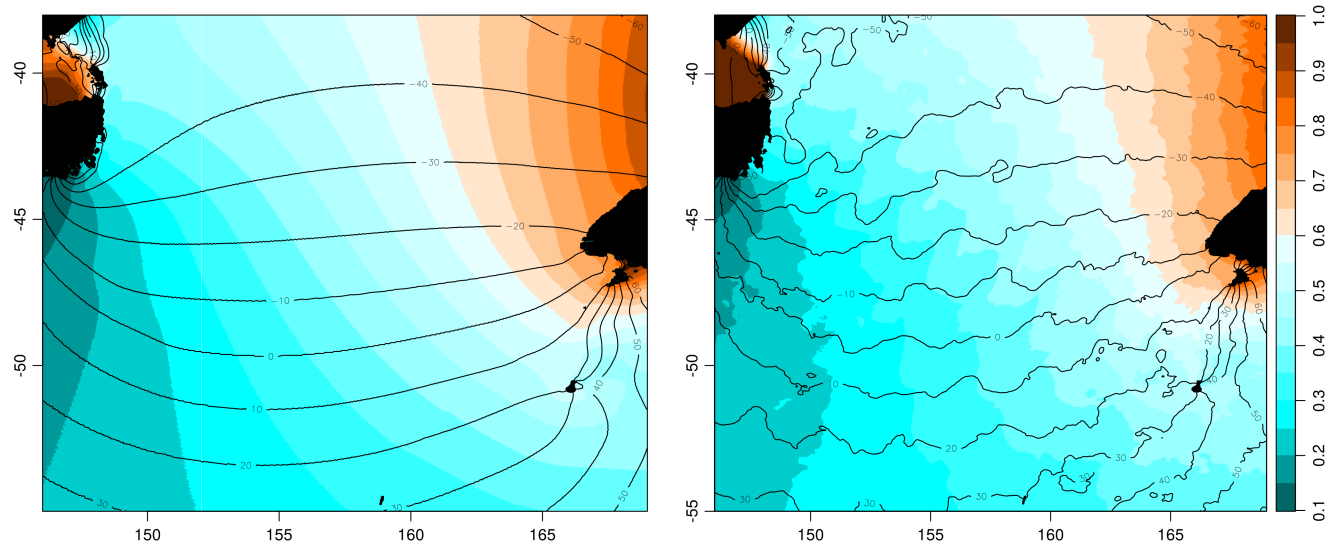


Figure 2: Comparison of M_2 sea level oscillations simulated by ROMS (left panel) with TPXO-model (right panel).

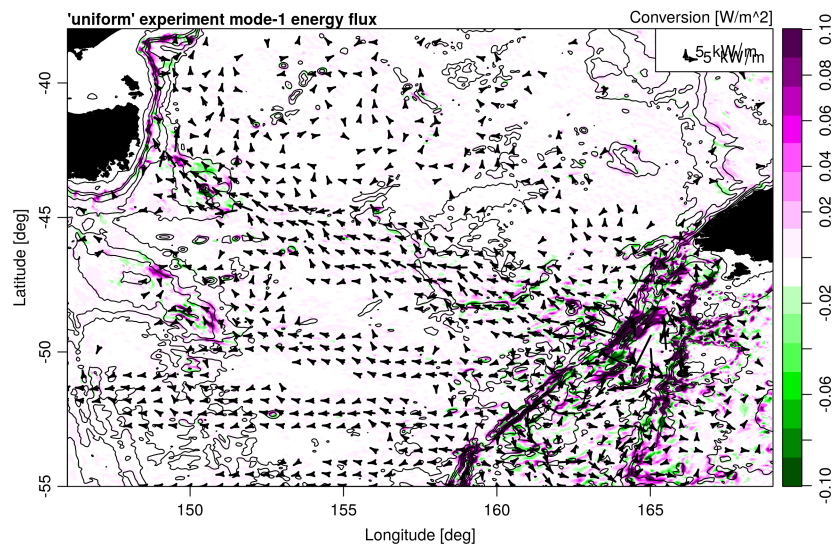


Figure 3: Beam of Tasman Sea with major internal tide production sites identified by superposed heat map.

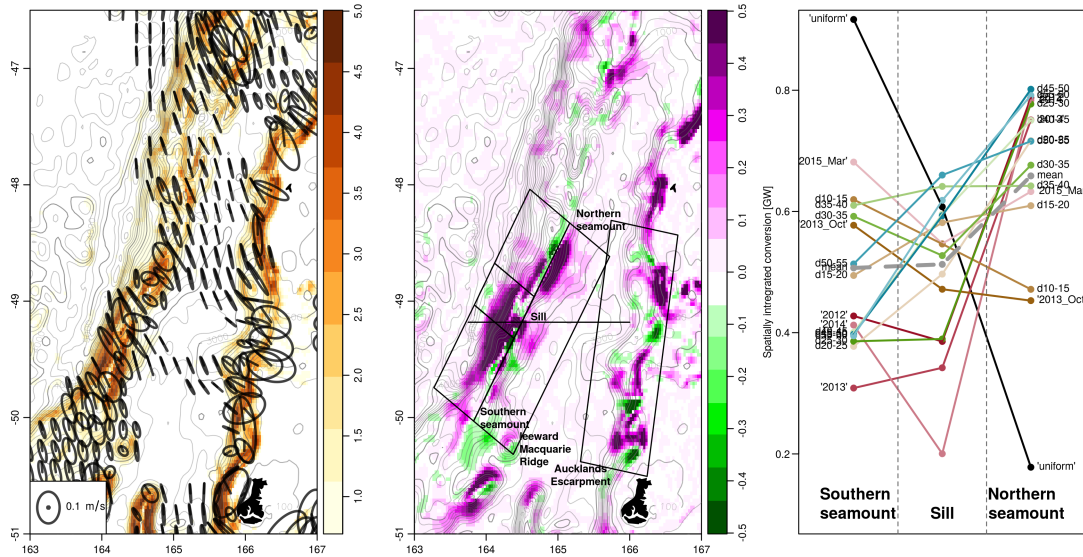


Figure 4: Generation of internal tides at Macquarie Ridge. (a) The heatmap illustrates criticality in the region of major generation. And ellipses are representative of barotropic current. (b) The diagnosed conversion rates for 'uniform' experiment. The boxes outline regions used in further analysis. (c) Variability of conversion rates in the three regions identified on the previous panel.

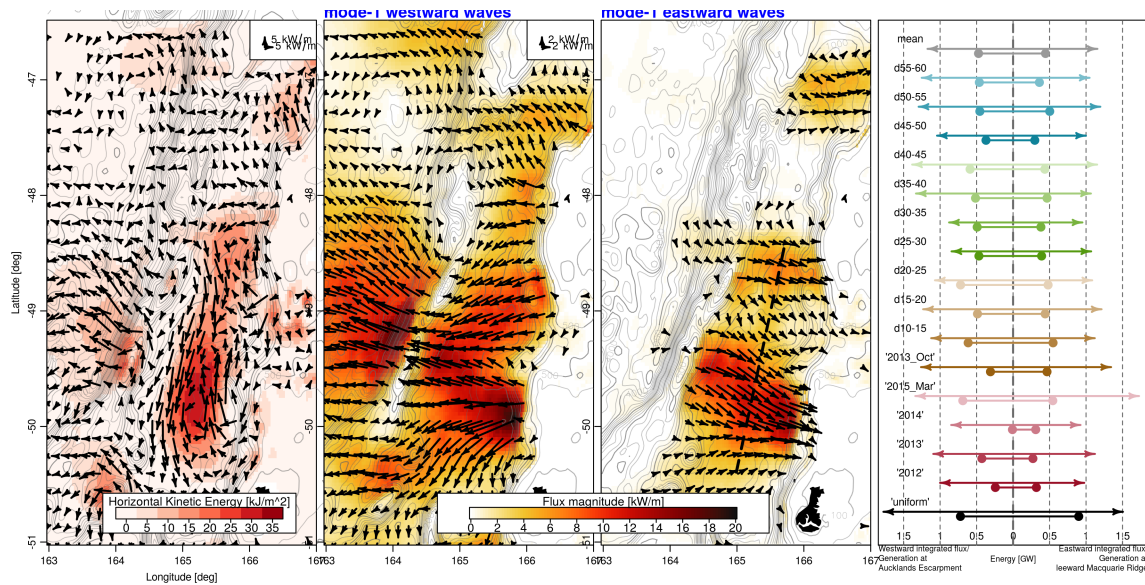


Figure 5: Standing wave between Macquarie Ridge and Auckland Escarpments. (a) Distribution of horizontal kinetic energy in 'uniform' simulation with overlaid energy flux of total mode-1 field. (b) Energy flux map of the westward component and the eastward component (c). Variation in energy characteristics of mode-1 field between Macquarie Ridge and Auckland Escarpment. The integrated flux was obtained for a dashed transect in (c) and is given by arrows. Dots show conversion rates spatially integrated over boxes given on (Fig. 4, b).

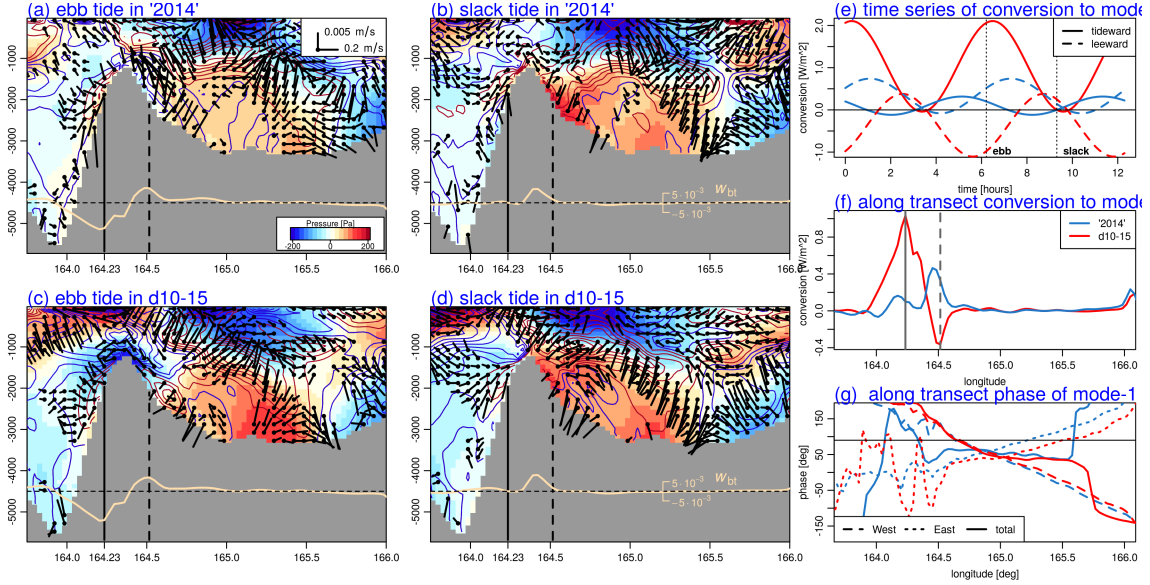


Figure 6: Distribution of baroclinic fields during ebb and slack tide along transect crossing Macquarie Ridge on Fig. 4, (b). (a-d) Baroclinic pressure anomaly with superposed isopycnal displacements given by contour lines. Positive color is assigned to lifted interfaces and negative - for the opposite. Stick lines show currents. And white line is distribution of barotropic velocity. The tideward and leeward sides of Macquarie Ridge are identified by vertical solid and dashed lines. On (e) it is shown time progression of baroptropic-to-baroclinic conversion for both experiments and ridge sides. While (f) gives distribution of period averaged conversion rate along the transect. The same is for (g) where progression of mode-1 baroclinic pressure is shown by phases of total field and elemental components. The phases are referenced to flood current across the sill.

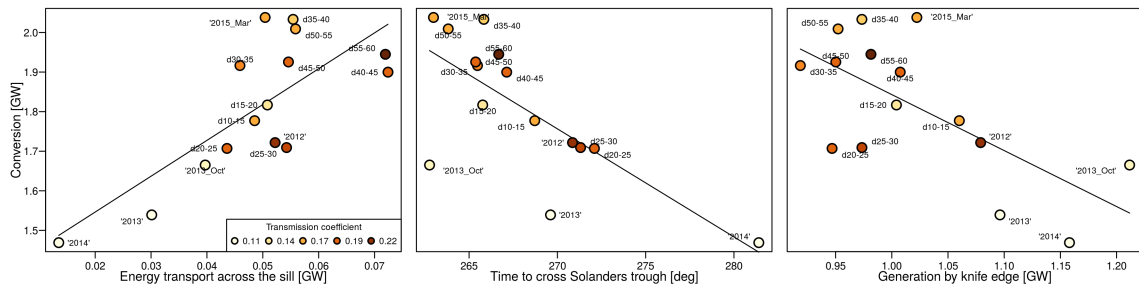


Figure 7: Variation of the tideward conversion rates in relation to mode-1 energy transmitted across the sill (a), to travel time across Solanders Trough (b), to knife-edge barrier representative of Macquarie Ridge seeing from the deep ocean.

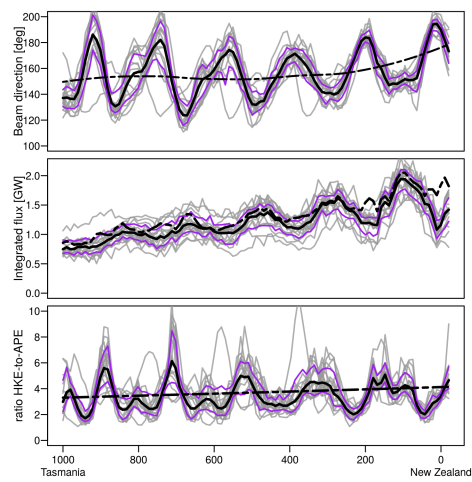


Figure 8: Along beam variation of across averaged energy characteristics. For all panels - solid black line is mean value and thin gray lines for each particular realization. Purple lines show mean deviation of realizations for mean. (a) Direction of energy flux. The dashed line is produced by regression with second order polynomial. (b) Integrated flux carried by the beam. Here the dashed line shows mean integrated flux with no account for relative angle with respect to across beam surface. (c) Ratio between horizontal kinetic energy to available potential energy. The dashed line is the ratio for a plane wave.

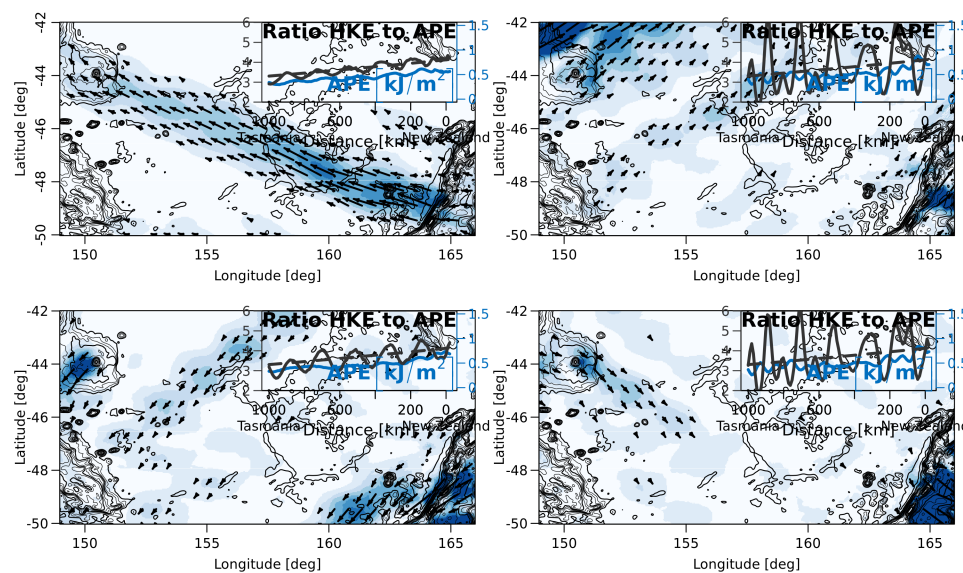


Figure 9: Superposition of multiple waves.

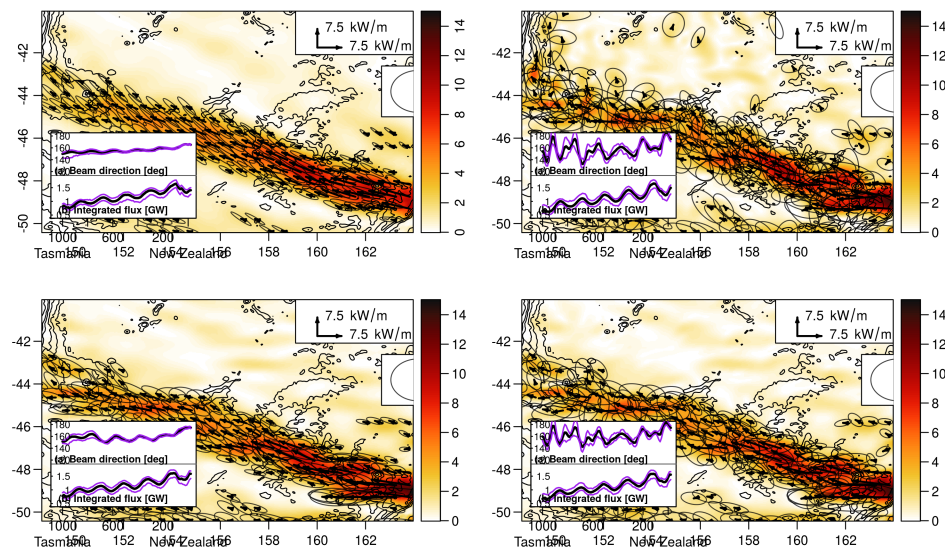


Figure 10: Variation of the beam.

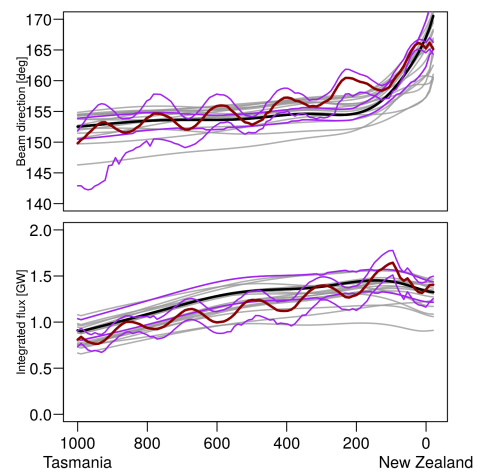


Figure 11: Variation of beam parameters.